Journal of Science and Technology – Smart Systems and Devices
Volume x, Issue x, Month Year, ppp–ppp

Influence of Cell Membrane Permeability on Moisture Diffusion in Plant Materials During Convective Drying Process

Hoang Vu Tuyen, Hiep Le Kieu*
Hanoi University of Science and Technology, Ha Noi, Vietnam
**Corresponding author email: hiep.lekieu@hust.edu.vn*

Abstract
In this study, a continuum model is developed to describe the heat and mass transfer processes within a cellular-structured plant medium during hot-air drying at atmospheric pressure. The model accounts for the convective flow of the liquid and vapor phases through the inter-cellular void spaces, as well as the diffusive flow of the liquid phase across the solid cell membranes of the porous material. The numerical solution of the model is verified through global mass and energy balance checks, as well as through examination of the limiting behavior of the water conductivity of the cell membrane, confirming the physical consistency of the model; An assessment of the model's accuracy was performed to evaluate the grid's independence from the pressure distribution across the entire sample thickness, showing that the model was independent of grid variation; comprehensive validation against experimental drying data has not yet been performed and is identified as a direction for future work. Based on the constructed model, the influence of the water conductivity of the cell membrane on the spatial and temporal distributions of temperature and moisture content within the porous medium is also preliminarily investigated. The results indicate that the diffusion of water through the cell membrane governs the heat and mass transfer dynamics within the porous material and therefore determines the kinetics of the drying process.

Keywords: Cell membrane permeability, continuum model, heat and mass transfer, porous media, potato drying.

1. Introduction

The drying of materials with complex cellular structures is a physical problem involving coupled heat and mass transfer in a multiphase system in which the material undergoes structural changes and shrinkage throughout the drying process. The typical structure of a material with a microscale cellular architecture in general and plant cellular tissue in particular is described in Figs. 1 and 2 comprising four distinct phases: the vacuole, cytoplasm, cell wall and extracellular space [1]. The extracellular space is an interconnected air-filled void between cells, surrounded by the outer cell membrane. In epithelial tissue, it is referred to as the intercellular cleft and typically ranges from 25 to 35 nm in width, filled with fluid [2]. In the present model, the vacuole and cytoplasm are grouped into a single intracellular region, while the extracellular space represents the intercellular region outside the cells. Accordingly, the four physical components identified in the cellular structure are represented by two moisture-transport regions in the continuum model: intracellular and extracellular.

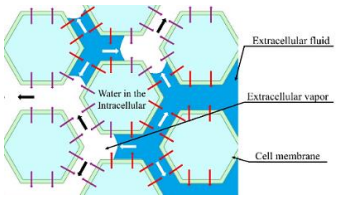


Fig. 1. The movement of liquid flow throughout the drying process in a porous medium structure. White and black arrows represent the liquid and vapor fluxes moving in the extracellular region, respectively. Purple and red arrows describe the diffusive water flux across the cell membrane

It can thus be observed that the liquid component in dried materials with cellular microstructures exhibits a relatively complex distribution that cannot be adequately described solely through predictive models of average moisture content variation over time. Instead, this research must delve deeper into analyzing liquid flow and evaporation processes within plant porous media possessing cellular structures. This is attributed to the simplification in which the transport resistance of liquid-vapor flow in the intracellular space and across the cell membrane is lumped into an effective diffusion coefficient, which serves as a single calibration parameter. This simplification gives rise to significant discrepancies between mathematical models and actual drying processes.

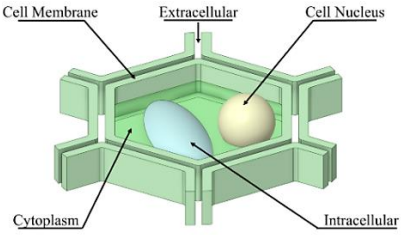


Fig. 2. The structure of a plant cell

The moisture diffusion and heat transfer processes in porous materials with cellular microstructures have been increasingly studied for a wide variety of drying agents. These models are constructed at multiple scales, which can be illustrated through the works of various authors, such as at the microscale level [3]; the mesoscale level [4]; the macroscale level (corresponding to a single slice) [5]; however, most theoretical models investigating the influence and

p-ISSN 3093-3285
e-ISSN 3093-3315
https://doi.org/10.51316/jst.xxx.ssad.xxxx.xx.x.x
Received: Jul 16, 2026; Revised: Aug 17, 2026;
Accepted: Oct 13, 2026; Online: Nov 18, 2026

In press

development of drying models using hot air as the drying agent for porous materials with cellular microstructures have thus far focused only on constructing moisture diffusion models and heat transfer models under the assumption that there is no interaction between moisture components of the extracellular space and the intracellular space, and typically treat the porous cells as isolated entities [6]. This may render the model physically inaccurate, as factors influencing the drying process, which include the cell wall, surface permeability, and the pressure differential between the two liquid phases present in the material, would be neglected and not explicitly represented. For the reasons outlined above, this study aims to address issues related to heat and mass transfer processes at the microscale level, serving as a foundational step toward the construction and development of a comprehensive mathematical model for future research.

2. Model Description

In this study, the drying process of materials with parenchymal tissue cell structures is investigated. For this type of structure, moisture within the plant tissue is distributed both in the intracellular space (also referred to as the intracellular region) and in the capillary spaces between cells (also referred to as the extracellular space), as illustrated in Fig. 1.

The void space between cells contains either a liquid phase or a vapor phase [2]. Under the influence of capillary forces and pressure differentials between spatial regions, two diffusive fluxes are formed from the intracellular to the extracellular space, which include the moisture flux in the liquid phase and the moisture flux in the vapor phase passing through the cell membrane. To construct a mathematical model of the plant material drying process, several assumptions are adopted. First, the water inside the material is assumed to be pure. The temperature of water, water vapor, and the solid fraction at any point within the material are assumed to be equal, meaning that the internal phases of the material are in thermal equilibrium. Additionally, solutes inside the cells are assumed to be stationary, with only water molecules being capable of passing through the cell membrane. The final assumption is that the moisture flux between two adjacent cells is neglected.

2.1. Mass Conservation Equation

The variation in extracellular water content within a volume element during the drying process is represented by mass transfer mechanisms, which include the convective movement of liquid flow, the phase change of liquid into vapor, and the diffusion of liquid water across the cell membrane.

$$\rho_l \frac{\partial \varepsilon_{l,ex}}{\partial t} + \rho_l \nabla \cdot \left(v_{l,ex}\right) + \dot{m}_v = j_{w,1} A_v \frac{\varepsilon_{l,ex}}{\varepsilon_{l,ex}+\varepsilon_{g,ex}} \quad (1)$$

where $\varepsilon_{l,ex} = \frac{V_{l,ex}}{V}$, $\varepsilon_{g,ex} = \frac{V_{g,ex}}{V}$ are the volume fractions occupied by extracellular liquid water and by vapor, respectively, relative to the total volume; $\dot{m}_v(\mathrm{kg/m^3}s)$ denotes the mass of liquid evaporated per unit volume per second and $j_{w,1}\left(\mathrm{kg/m^2 s}\right)$ is the flux of water diffusing through the cell membrane surface per second; $v_{l,ex}$ is the Darcy velocity of the liquid flow in the intracellular void space and $\rho_l\left(\mathrm{kg/m^3}\right)$ is the density of the liquid component; $A_v\ (m^2/m^3)$ denotes the specific surface area per unit volume, which also represents the cell surface area per unit volume. Parameter $A_v \frac{\varepsilon_{l,ex}}{\varepsilon_{l,ex}+\varepsilon_{g,ex}}$ characterizes the cell surface area covered by liquid water, in which $\psi = \varepsilon_{l,ex} + \varepsilon_{g,ex}$ describes the porosity of the void space between cells within the medium.

Regarding the vapor transport process in the gas phase, the variation of extracellular vapor within a volume element is driven by the convective movement of the vapor flux and the amount of vapor generated through evaporation $\dot{m}_v$ and the flux of water vapor diffusing through the cell wall $j_{w,2}\ (kg/m^2 s)$ acting as sources of vapor generation. Therefore, the mass conservation equation for extracellular water vapor can be written in the form of Equation (2).

$$\frac{\partial(\rho_v \varepsilon_g)}{\partial t} + \nabla \cdot \left(\rho_v v_g\right) - \dot{m}_v - \nabla \cdot \left(\rho_g . D_{eff} . \nabla \left(\frac{\rho_v}{\rho_g} \right) \right) = j_{w,2} A_v \frac{\varepsilon_{v,ex}}{\varepsilon_{l,ex}+\varepsilon_{g,ex}} \quad (2)$$

where v_g is the Darcy velocity of the gas flow in the extracellular void space and $\rho_v\ (kg/m^3)$ is the density of the vapor phase and $\rho_g\ (kg/m^3)$ is the density of air; D_{eff} is the effective diffusion coefficient.

By combining both (1) and (2), the mass conservation equation for the liquid and vapor components in the extracellular region is written in the form of (3).

$$\rho_l \frac{\partial \varepsilon_{l,ex}}{\partial t} + \rho_l \nabla . \left(v_{l,ex}\right) + \frac{\partial(\rho_v \varepsilon_g)}{\partial t} + \nabla \cdot \left(\rho_v v_g\right) - \nabla \cdot \left(\rho_g . D_{eff} . \nabla \left(\frac{\rho_v}{\rho_g} \right) \right) = j_{w,1} A_v \frac{\varepsilon_{l,ex}}{\varepsilon_{l,ex}+\varepsilon_{g,ex}} + j_{w,2} A_v \frac{\varepsilon_{g,ex}}{\varepsilon_{l,ex}+\varepsilon_{g,ex}} \quad (3)$$

In press

Similarly, the mass conservation equation for moisture within the intracellular region is established and can be written in the form of (4).

$$\rho_l \frac{\partial \varepsilon_{l,in}}{\partial t} + j_{w,1} A_v \frac{\varepsilon_{l,ex}}{\varepsilon_{l,ex} + \varepsilon_{g,ex}} + j_{w,2} A_v \frac{\varepsilon_{g,ex}}{\varepsilon_{l,ex} + \varepsilon_{g,ex}} = 0 \quad (4)$$

The mass transfer process for the extracellular air component follows the vapor diffusion from the surface into the vacuolar space and is described by (5).

$$\frac{\partial}{\partial t}\left(\rho_a \varepsilon_g\right) + \nabla \cdot \left(\rho_a v_g\right) - \nabla \cdot \left(\rho_g D_{eff} \nabla \left(\frac{\rho_a}{\rho_g} \right) \right) = 0 \quad (5)$$

Where $\varepsilon_{l,in} = \frac{V_{l,in}}{V}$ is the volume fraction occupied by intracellular liquid water and ρ_a (kg/m^3) is the density of the gas component.

2.2. Energy Conservation Equation

Thermal energy is transferred into the volume element through two primary mechanisms: heat conduction and convective heat exchange. This energy is utilized for the evaporation process and for heating the porous material medium. Based on the local thermal equilibrium assumption, the energy conservation equation can be written in the form of (6).

$$\left\langle \rho C_p \right\rangle \frac{\partial T}{\partial t} + \left[\rho_l c_{p,l} v_{l,ex} + \rho_v^g c_{p,g} v_{g,ex} \right] \cdot \nabla T = \nabla \cdot \left(\lambda_{eff} \nabla T \right) - \Delta h_{evp} \left(\dot{m}_v + j_{w,2} A_v \frac{\varepsilon_{v,ex}}{\varepsilon_{l,ex} + \varepsilon_{v,ex}} \right) \quad (6)$$

Where Δh_v is the latent heat of vaporization; $\left\langle \rho C_p \right\rangle$ is the effective isobaric specific heat capacity, determined through (7).

$$\left\langle \rho C_p \right\rangle = \varepsilon_s \rho_s c_{p,s} + \left(\varepsilon_{l,ex} + \varepsilon_{l,in}\right) \rho_l c_{p,l} + \varepsilon_g \rho_v c_{p,v} + \varepsilon_g \rho_a c_{p,a} \quad (7)$$

Thus, based on (3)–(6), which have been established to describe the heat and mass transfer processes between the drying material, which is a biological material with a porous structure, and the drying agent, which is hot air, a system of differential equations is formed comprising four equations and four unknowns. Specifically, the four governing unknowns are the total gas pressure in the extracellular void space, p_g; the partial pressure of water vapor in the extracellular gas phase, p_v; the temperature of the porous medium, T; and the intracellular liquid moisture content, X_{in}. (3–6), which represent the combined extracellular liquid-and-vapor mass balance, the extracellular vapor (moist-air) mass balance, the intracellular moisture balance, and the energy balance, respectively, provide the four corresponding conservation statements used to solve for these four unknowns at each grid node. The system is closed through the constitutive relations listed in Table 1, in which the extracellular liquid volume fraction $\varepsilon_{l,ex}$, and hence the liquid pressure $p_{l,ex}$, is obtained from p(g) via the capillary pressure–saturation relationship, the Darcy velocities $v_{l,ex}$ and $v_{g,ex}$ follow from $p_{l,ex}$ and $p_{g,ex}$ through the generalized Darcy's law with the corresponding relative permeabilities, and the vapor density ρ_v is related to ρ_v through the ideal-gas law.

2.3. Constitutive Equations

The constitutive equations relating to the fluxes and the flow equations that serve as the basis for computing and solving the conservation differential equations are presented in Table 2.

In this study, the influence of cell membrane permeability will be evaluated in greater detail in the results section of this work, as the cell membrane begins to rupture at high temperatures, according to the study by Halder *et al.* [7]. In this section, the impact of the water conductivity of the cell membrane, k_p, is investigated. However, to the authors' knowledge, as also mentioned in Halder's study, determining the value of the water conductivity of the cell membrane throughout the drying process is not yet feasible, since the breakdown of the cell membrane structure at high temperatures (50°C for potato-based material) is extremely difficult to characterize. Therefore, to evaluate the influence of kp on the drying characteristics, numerical simulations were performed for three different values of kp, varying by several orders of magnitude from $k_p\left(20^o C\right) = 1.8 \times 10^{15}\ m^3/Ns$ to $10^3 \times k_p\left(20^o C\right)$ [8].

2.4. Initial and Boundary Conditions

The drying sample is treated as a flat plate of thickness, with an initially uniform temperature T_0 and a uniformly distributed moisture content throughout the sample X_0. The drying sample is subjected to convective hot air flow from both sides, with a uniform ambient temperature of T_f and pressure p_f. Due to the symmetry of the drying sample, it can be treated as a perfect mirror, meaning that the computational domain of interest is reduced to only one half of the plate, as shown in Fig. 3.

In press

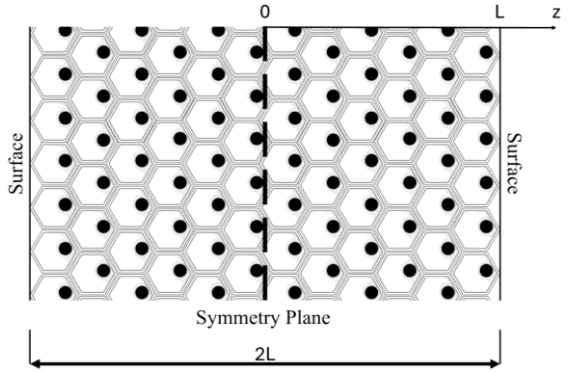


Fig. 3. Schematic diagram of the drying sample and its coordinate system

At the exposed surface of the flat plate $z = L$ with respect to the temperature of the drying material, a third-kind boundary condition, also known as a Robin boundary condition, is applied. This boundary condition accounts for the convective heat exchange between the drying surface and the surrounding environment.

$$[\lambda_{eff}\ \frac{\partial T}{\partial z} + \Delta h_{evp}\rho_l v_{l,ex} + h_{evp}\left(\rho_l v_{l,ex} + \rho_g v_{g,ex}\right) = \alpha\left(T_f - T_{surf}\right) \tag{8}$$

Where z is the coordinate in the direction perpendicular to the plane of the plate; $\alpha\ (W/m^2K)$ is the total heat transfer coefficient on the gas side, which includes both convective and radiative heat transfer.

Due to the large mass transfer coefficient at the exposed surface [9], the vapor pressure at the exposed surface is assumed to equal the ambient pressure throughout the drying process.

$$p_v\,|_{z=L} = \varphi p_{v,sat}(T_f) \tag{9}$$

At the plane of symmetry, symmetric boundary conditions are applied to both heat and mass transfer, as defined by (10).

$$\frac{\partial T}{\partial z}\,|_{z=0} = 0 \ \text{ and } \ \frac{\partial v_{l/g,ex}}{\partial z}\,|_{z=0} = 0 \tag{10}$$

The mass and energy conservation equations are discretized into a system of algebraic equations for each grid node [10]. A MATLAB program is developed to iteratively solve the system of equations using the built-in function ODE15s [11] through the finite volume method. To ensure numerical convergence, simulations are performed on multiple grids consisting of 21, 41, 51, 61, and 101 nodes. When the number of nodes exceeds 51, the numerical solution becomes grid-independent (not shown here). Therefore, 51 nodes are used for all simulations.

2.5. Thermophysical Parameters of the Material

The thermophysical properties of potato, as well as those of water vapor and liquid water, are listed in Table 3 and Table 4, respectively. The boundary conditions of the simulation are listed in Table 1.

The thermophysical properties of liquid water and water vapor are determined based on the water phase diagram, which characterizes the thermodynamic state of water as a function of temperature and pressure. In the temperature range relevant to the drying process investigated in this study, two principal thermodynamic states are considered: liquid water in the saturated state (on the saturated liquid curve) and water vapor in the saturated state (on the saturated vapor curve). The corresponding thermophysical properties, including density, dynamic viscosity, thermal conductivity, specific heat capacity, and the latent heat of vaporization, are obtained from the saturated-state property tables reported in the VDI Heat Atlas [12] and are expressed as second-order polynomial functions of temperature, with the regression coefficients determined by the least-squares method over the temperature range relevant to this study.

Table 1. Boundary condition parameters

Parameter	Value
Half-Sample thickness	$2(mm)$
Initial temperature T_0	20^oC
Initial moisture content X_0	$4.8 kg_w / kg_{db}$
Drying agent temperature T_f	$40-80°C$
Air velocity v	$0.33 m/s$
ODE15s absolute tolerance AbsTol	10^{-8}
ODE15s relative tolerance RelTol	10^{-6}
Output time step $\Delta\tau$	$0.1(s)$
Number of grid nodes N	51

Using the data table provided, the thermophysical properties are approximated by means of the least-squares method in the form of a second-order polynomial function.

$$y = a + bx + cx^2 \tag{51}$$

The coefficients a, b, and c are determined by solving the system of equations below.

$$\begin{aligned} &na + \Sigma x_i b + \Sigma x_i^2 c = \Sigma y_i \\ &\Sigma x_i + \Sigma x_i^2 b + \Sigma x_i^3 c = \Sigma x_i y_i \\ &\Sigma x_i^2 a + \Sigma x_i^3 b + \Sigma x_i^4 c = \Sigma x_i^3 y_i \end{aligned} \tag{52}$$

From the above, the following empirical correlations include the specific heat capacity of the air are obtained in Table 4.

In press

Table 2. Flux equations and flow equations

Parameter	Values/Equations	
Liquid phase surface velocity or Darcy velocity $v_{l,ex}$ [10]	$v_{l,ex} = -\frac{KK_{r,l}}{\mu_l}\nabla p_{l,ex}$	(11)
Air phase surface velocity or Darcy velocity $v_{g,ex}$ [10]	$v_{g,ex} = -\frac{KK_{r,g}}{\mu_g}\nabla p_{g,ex}$	(12)
Relative permeability of the liquid phase and gas phase [13]	$K_{r,l} = \left(\frac{\varepsilon_{l,ex}}{\psi}\right)^2$ and $K_{r,g} = \left(1-\frac{\varepsilon_{g,ex}}{\psi}\right)^2$	(13)
Relationship between liquid pressure and vapor pressure [14]	$p_c\left(\varepsilon_{l,ex}\right) = p_g - p_{l,ex}$	(14)
Capillary pressure $p_c\left(\varepsilon_{l,ex}\right)$ [8]	$p_c\left(\varepsilon_{l,ex}\right) = \frac{4.\sigma(T)}{d_{pore}}$	(15)
Vapor pressure p_v [10]	$p_v = \varphi\left(X_{ex}, T\right) * p_{v,sat}$	(16)
Extracellular moisture content of the porous sample X_{ex} [8]	$X_{ex} = \frac{\varepsilon_{l,ex}\rho_l}{\varepsilon_s\rho_s}$	(17)
Saturated vapor pressure $p_{v,sat}$ [12]	$p_{v,sat}(T[^oC]) = exp(23.426 - \frac{3978.205}{233.349 + T[^oC]})$	(18)
Effective vapor diffusion coefficient D_{eff} [15]	$D_{eff}(S,T,P) = (1-S)\psi\delta_{va}$	(19)
Binary diffusion coefficient δ_{va} [16]	$\delta_{va}\left(T,P\right) = 2.26 * 10^{-5}.\left(\frac{T}{T_R}\right)^{1.81}\frac{P_R}{P_g}$	(20)
Effective thermal conductivity coefficient λ_{eff} [17]	$\lambda_{eff} = \varepsilon_s\lambda_s + \varepsilon_l\lambda_l$	(21)
Water flux diffusing through the cell membrane $j_{w,1}$	$j_{w,1} = -\rho_l k_p(\phi_{w,in} - \phi_{l,ex})$	(22)
Vapour flux diffusing through the cell membrane $j_{w,2}$	$j_{w,2} = -\rho_l k_p(\phi_{w,in} - \phi_{g,ex})$	(23)
Water conductivity of the cell membrane k_p [8]	$k_p(20\ ^oC)\ =\ 1.8 \times 10^{15}$ m^3/Ns to $10^3 \times k_p(20^oC)$ m^3/Ns	(24)
Water potential function within the cell $\phi_{w,in}$ [18]	$\phi_{w,in} = 10^6\ (7.8\frac{X_{in}}{X_{in,0}} - 7.8003)$	(25)
Extracellular capillary potential function $\phi_{l,ex}$ [19]	$\phi_{l,ex} = -p_c$	(26)
Moist air potential function in the vacuolar space $\phi_{g,ex}$ [19]	$\phi_{g,ex} = \frac{\tilde{R}T\rho_l}{\tilde{M}_w} ln\left(\frac{p_{v,ex}}{p_{v,sat}}\right)$	(27)

Table 3. Thermophysical parameters of the potato sample

Parameter	Values/Equations	
Absolute permeability, K [18]	$4.168 \times 10^{-12}\ m^2$	(28)
Specific cell surface area per unit volume, A_v [18]	10885.62 m^2 / m^3 with effective cell size 100 μm	(29)
Total Porosity, ψ [18]	0.0389	(30)

In press

Parameter	Values/Equations	
Pore size distribution [18]	$T_f = 80^{\circ}\text{C}, \quad w = 0.33$ m/s và $X_0 = 4.8$ kg$_w$/kg$_{db}$ $f = -1.313\times10^{-6}d^4 + 1.172\times10^{-4}d^3$ $-3.371\times10^{-3}d^2 + 3.329\times10^{-2}d$ -2.546×10^{-2} With $d_{min} = 2.9\ \mu m$ and $d_{max} = 29.49\ \mu m$	(31)
Capillary pressure, p_c	$p_c\left(\varepsilon_{l,ex}\right) = \dfrac{4\sigma(T)}{d}$ Where $\varepsilon_{l,ex} = \psi \dfrac{\int_{d_{min}}^{d} \frac{\pi d^2}{4} f d(d)}{\int_{d_{min}}^{dmax} \frac{\pi d^2}{4} f d(d)}$	(32)
Sorption isotherm [14]	$X = \dfrac{b_o b_1 b_2 \varphi}{(1-b_1\varphi)(1-b_1\varphi+b_1 b_2\varphi)}$ $b_1 = b_{10}\exp\left(\dfrac{b_{11}}{RT[K]}\right),\ b_2 = b_{20}\exp\left(\dfrac{b_{21}}{RT[K]}\right)$ $b_0 = 8.7,\ b_{10} = 1.86\times10^{-5}, b_{11} = 34.1$ $b_{20} = 5.86, \quad b_{21} = 6.75$	(33)
Solid phase density, ρ_s [20]	$262.101 kg/m^3$	(34)
Specific heat capacity of the solid phase, $c_{p,s}$ [20]	$1699 + 6.1\,T\,[^oC] J/kgK$	(35)
Thermal conductivity of the solid phase, λ_s [21]	$0.327 W/mK$	(36)
Thermal emissivity δ [22]	0.89	(37)

Table 4. Thermophysical parameters of water and moist air

Parameter	Values/Equations	
Specific heat capacity of water $c_{p,l}$ [12]	$c_{p,l} = 4.207552 - 1.528042\times10^{-3}t + 1.730769\times10^{-5}t^2\ \left[kJ/kgK\right]$	(38)
Specific heat capacity of air $c_{p,g}$	$\varepsilon_g c_{p.v} + \varepsilon_a c_{p.a}\ kJ/kgK$	(39)
Specific heat capacity of dry air $c_{p,a}$ [12]	$c_{p,a} = 1.004441 - 3.123543\times10^{-5}t + 2.331002\times10^{-7}t^2\ \left[kJ/kgK\right]$	(40)
Specific heat capacity of vapor $c_{p,v}$ [12]	$c_{p,v} = 1.85849 - 4.445221\times10^{-5}t + 1.714452\times10^{-5}t^2\ \left[kJ/kgK\right]$	(41)
Density of water ρ_l [12]	$\rho_l = 1000.544 - 6.969464\times10^{-2}t - 3.567599\times10^{-3}t^2\left[kg/m^3\right]$	(42)
Density of moist air ρ_g	$\rho_g = \rho_a + \rho_v\ kg/m^3$	(43)
Density of dry air ρ_a [12]	$\rho_a = 1.291601 - 4.503730\times10^{-3}t - 1.058275\times10^{-5}t^2\left[kg/m^3\right]$	(44)
Density of vapour ρ_v [12]	$0.598\dfrac{\rho_v}{p_{v,sat}(t^oC)}\dfrac{373.15}{T[K]}\ kg/m^3$	(45)
Dynamic Viscosity of water μ_l [12]	$\mu_l = 1.665936\times10^{-3} - 3.242689\times10^{-5}t + 1.932389\times10^{-7}t^2\left[N.s/m^2\right]$	(46)
Dynamic Viscosity of moist air μ_g [23]	$\mu_g = 1{,}716\times10^{-5}\left(\dfrac{T[K]}{273{,}15}\right)^{3/2}\dfrac{383.55}{T[K]+110.4}\left[N.s/m^2\right]$	(47)
Thermal conductivity of liquid λ_l [12]	$\lambda_l = 0.5513287 + 2.562634\times10^{-3}t - 1.259907\times10^{-5}t^2\left[W/mK\right]$	(48)
Latent heat of vaporization Δh_{evp} [12]	$\Delta h_{evp} = 2500.063 - 2.288438t - 1.351981\times10^{-3}t^2\left[kJ/kg\right]$	(49)
Surface tension σ [10]	$\sigma(T[^{\circ}\text{C}]) = 1.3\times10^{-7}T^2 - 1.58\times10^{-4}T + 0.076$ N/m	(50)

In press

3. Simulation Results and Discussion

3.1. Model Evaluation

The simulation results of temperature and moisture content of the drying sample are consistent with the drying behavior described in the literature, which divides the drying process into three stages with distinct heat and mass transfer mechanisms, as illustrated in Fig. 4.

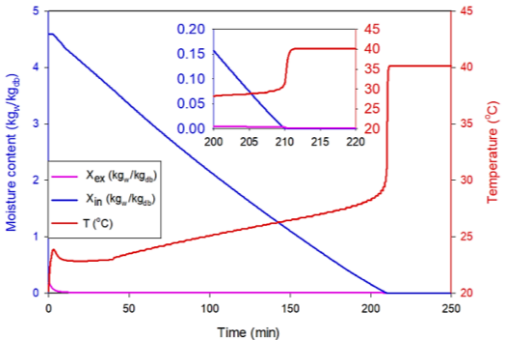


Fig. 4. Graph of temperature and moisture content as a function of time under drying conditions $T_f = 40^{\circ}\mathrm{C}, X_o = 4.8\ \mathrm{kg_w/kg_{db}}, k_p = k_P^0$ and drying time $\tau = 250$ min

During the first drying stage (0–5 min), the material undergoes a heating phase, which can be described directly through two energy fluxes, namely the latent heat and the sensible heat. These two energy fluxes are supplied to the drying material, driving its temperature up to the saturation temperature of water vapor. Regarding the mass transfer process in this stage, the migration of moisture from the intracellular space to the extracellular space occurs under the influence of capillary forces and the pressure differential between the interior and exterior regions of the cell. The equilibrium of the moisture distribution in the extracellular region is disrupted only when the moisture content inside the cell reaches an equilibrium state, at which point the moisture within the intracellular space is no longer capable of migrating outward, causing the evaporation process to be interrupted This leads to the gradual disappearance of the latent heat component, and the temperature can no longer be maintained at the saturation temperature, instead tending to shift toward a new equilibrium temperature approximately equal to that of the drying agent. This also marks the third stage of the drying process.

Fig. 5 shows the temporal evolution of gas pressure at different positions along the thickness of the sample during the drying process. It can be observed that at all positions, the pressure initially increases gradually, reaches a maximum value after approximately 60–70 minutes, and then rapidly decreases back toward ambient pressure. This trend reflects the accumulation of water vapor within the capillary structure of the material during the evaporating stage, or the second drying stage, when the internal evaporation rate exceeds the capacity for moisture diffusion toward the surface. As the drying process continues, the formation and development of gas pathways or the displacement of the evaporation front toward the surface reduces the diffusion resistance, leading to a sudden decline in pressure.

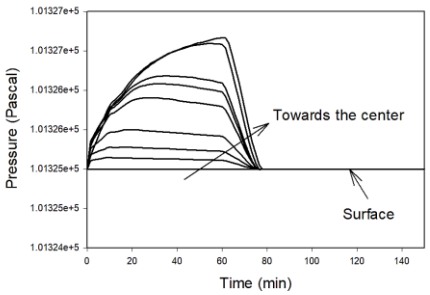


Fig. 5. The temporal variation of pressure at positions distributed along the thickness under drying conditions $T_f = 80^{\circ}\mathrm{C}, \ X_o = 4.8\mathrm{kg_w/kg_{db}}, k_p = k_P^0$

Furthermore, the relatively small pressure difference between the sample center and surface is physically consistent with the short characteristic flow length and the Darcy-type description of gas transport through the porous medium. In the present model, the characteristic half-thickness is only $L = 2\,mm$; therefore, even with a finite pressure gradient required to drive the gas flow, the resulting pressure drop across this short flow remains small. According to Darcy's law, the pressure gradient is related to the gas velocity as $\nabla p = -\mu_g u_g / K_g$, indicating that the pressure difference is directly dependent on the characteristic flow length. To further verify that the predicted pressure variation is not a numerical artifact, a grid-sensitivity analysis was performed by varying the number of spatial nodes. The maximum pressure and the corresponding time were compared for different spatial resolutions, as summarized in Table 5. The small variation in these quantities with increasing node number confirms that the predicted pressure behavior is essentially independent of the spatial discretization.

In Table 5 The maximum pressure and its corresponding occurrence time show only negligible variations with increasing grid resolution. This confirms that the predicted pressure response is essentially independent of the spatial discretization and demonstrates the numerical stability of the model.

Table 5. Grid sensitivity of the predicted pressure response

N	$p_{max}\,(Pa)$	$t_{max}\,(min)$
11	101326.63	63.08
21	101326.65	62.93
41	101326.67	62.77
51	101326.67	62.80
101	101326.68	62.77

In Press

3.2. Model Validation

3.2.1. Verification via limiting cases of water conductivity of the cell membrane

To verify the physical consistency of the proposed two-region formulation, two limiting cases of the water conductivity of the cell membrane, $k_p \to \infty$ and $k_p \to 0$, were examined.

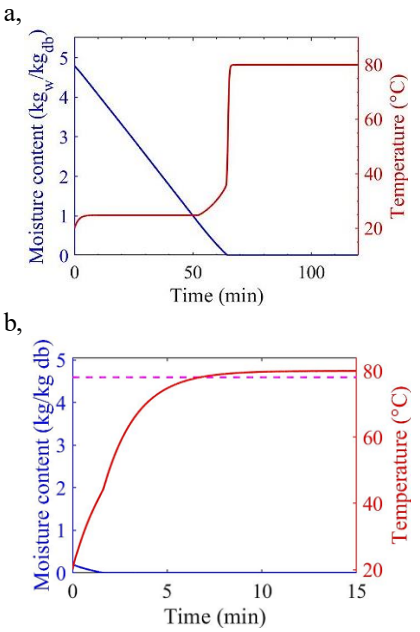


Fig. 6. Limiting cases of the proposed two-region model: (a) $k_p \to \infty$ and (b) $k_p \to 0$

When $k_p \to \infty$, the cell membrane offers negligible resistance to moisture transport, so the intracellular and extracellular liquid phases are expected to remain in continuous equilibrium throughout the drying process. Fig. 6 confirms this expectation: the simulated intracellular and extracellular moisture content curves coincide exactly at every time step. The total moisture content decreases nearly linearly from the initial value to zero within approximately 65 minutes, while the material temperature remains close to a low, nearly constant value for most of this period before rising sharply toward the drying-agent temperature (80 °C) once the moisture is exhausted. This behavior reproduces the classical constant-rate/falling-rate drying curve obtained from single-region (lumped) diffusion models, confirming that the present formulation correctly degenerates to the conventional case in the limit of a fully permeable membrane.

When $k_p \to 0$, the membrane becomes fully impermeable, the intracellular moisture is expected to remain trapped inside the cell for the entire drying process, while only the extracellular moisture can be removed by convective drying. Fig. 6 shows that the extracellular moisture content (blue curve) decreases sharply from its initial value to nearly zero within the first two minutes, whereas the intracellular moisture content (magenta dashed curve) remains essentially constant near its initial value of $4.8 kg_w / kg_{db}$ throughout the entire simulated period. This confirms that no measurable flux crosses the membrane under this condition, in agreement with the expected physical behavior. Correspondingly, the material temperature rises rapidly once the extracellular moisture has been removed, since evaporative cooling can no longer be sustained by the now-inaccessible intracellular water, reaching the drying-agent temperature within approximately seven minutes. This contrasts sharply with the sustained evaporation and the extended low-temperature period of about 65 minutes observed in the $k_p \to \infty$ case.

Taken together, these two limiting cases demonstrate that the model correctly recovers (i) the classical single-region diffusion behavior in the limit of vanishing membrane resistance, and (ii) complete confinement of intracellular moisture in the limit of an impermeable membrane, confirming that the coupled formulation is physically consistent at both at both limiting values of the water conductivity of the cell membrane.

3.2.2. Verification via mass and energy balance

To evaluate the numerical consistency of the proposed drying model, global mass and energy balances were performed over the entire drying period. Since the model is formulated on a one-dimensional basis, all quantities were evaluated per unit cross-sectional area. The mass balance was evaluated by comparing the initial water mass with the sum of the remaining water mass and the cumulative evaporated water mass, expressed as

$$M_{w,0} = M_w(t) + M_{evap}(t) \tag{53}$$

The corresponding relative mass-balance error was calculated as

$$\varepsilon_M = \left| \frac{\left[M_w(t_f) + M_{evap}(t_f) - M_{w,0} \right]}{M_{w,0}} \right| \times 100\% \tag{54}$$

Where t_f denotes the final drying time. Similarly, the energy balance was evaluated by comparing the cumulative convective heat supplied to the material with the corresponding sensible and latent energy contributions:

$$Q(t_f) \approx \Delta E_{sens}(t_f) + Q_{latent}(t_f) \tag{55}$$

The relative energy-balance error was subsequently determined as

$$\varepsilon_E = \left| \frac{\left[Q(t_f) - \Delta E_{sens}(t_f) - Q_{latent}(t_f) \right]}{Q(t_f)} \right| \times 100\% \tag{56}$$

Lower values of ε_M and ε_E indicate better conservation of mass and energy, respectively. These balance errors were calculated for each simulation condition and used to assess the numerical consistency

In press

of the model. The simulations were evaluated by varying the drying-air temperature T_f, initial moisture content X_o, and number of computational elements N, while the remaining model parameters were kept unchanged.

Table 6. Mass and energy balance errors for different simulation conditions

$T_f\,(°C)$	N	ε_M (%)	ε_E (%)
40	21	0.7205	1.6762
	41	0.3640	1.7186
	51	0.2914	1.7268
60	21	0.8382	1.6983
	41	0.4208	1.7373
	51	0.3336	1.7436
80	21	08938	1.7178
	41	0.4415	1.7530
	51	0.3554	1.7618

The energy balance error remains below 1.8% for all investigated cases and shows only a minor dependence on the number of grid nodes. This indicates that the numerical solution maintains a good level of energy conservation and that the calculated energy balance is relatively insensitive to spatial discretization.

3.3. Influence of Cell Membrane Permeability

At high drying temperatures, moisture transport pathways within the cellular porous medium may change because of temperature-dependent changes in cell membrane resistance [17]. In the present analysis, the effect of the water conductivity of the cell membrane, k_p, is examined using four values spanning three orders of magnitude: $k_p = k_p^0, 10k_p^0, 10^2 k_p^0$, and $10^3 k_p^0$. Figs. 7–9 are used to distinguish the effect of k_p on overall drying behavior from its effect on the partitioning and redistribution of moisture between the intracellular and extracellular regions.

Fig. 7 shows that changing k_p produces only a limited change in the overall drying trajectory under the conditions investigated. The total moisture content curves remain relatively close during the early and intermediate stages, indicating that the overall drying rate is less sensitive to k_p than the internal moisture distribution.

The difference becomes more apparent near the end of drying. From the numerical data, the time required for the total moisture content to fall below $0.01 kg_w\, kg_{db}^{-1}$ ranges from approximately $68.8 min$ for $k_p = 10^2 k_p^0$ to $72.8 min$ for $k_p = 10^3 k_p^0$. Thus, the variation in overall drying time is about 4 min, or approximately 6% of the total drying period. This confirms that drying time and overall drying rate are secondary effects of changing the water conductivity of the cell membrane in the present simulations.

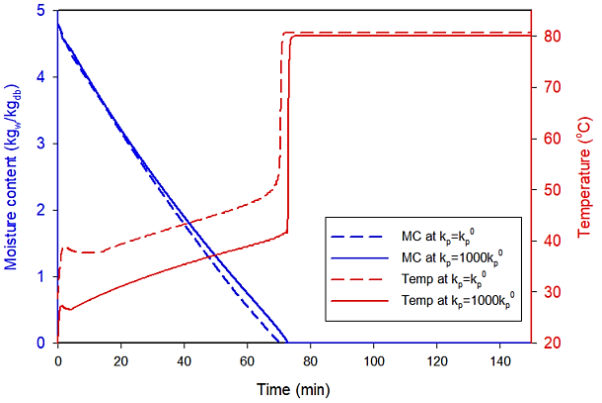


Fig. 7. Graph of temperature and moisture content as a function of time for the porous medium at two different values of water conductivity of the cell membrane, where the dot curve represents $k_p = k_p^0$ and the line curve represents $k_p = k_p^0 \times 10^2$; the drying agent temperature and the initial moisture content of the drying material are $T_f = 80^\circ C, X_o = 4.8\ \mathrm{kg_w/kg_{db}}$, respectively

The influence of k_p becomes much clearer when the intracellular moisture content is considered separately in Fig. 8(a). The four cases start from the same initial moisture content, but their intracellular moisture contents diverge rapidly during the early stage of drying. At approximately 10 min, the intracellular moisture contents are about $0.048, 0.040, 0.030$, and $0.008 kg_w\, kg_{db}^{-1}$ for $k_p = 10^3 k_p^0, 10k_p^0, 10^2 k_p^0$, and $k_p = k_p^0$, respectively. The substantially higher intracellular moisture retained at low k_p indicates that the cell membrane restricts water transport from the intracellular region to the extracellular region. Increasing k_p therefore promotes the redistribution of intracellular moisture toward the extracellular space. This effect is considerably stronger than the corresponding change in total moisture content shown in Fig. 8(b), demonstrating that k_p primarily controls the internal partitioning of moisture rather than the overall amount of water removed from the sample.

Fig. 9(a) shows the corresponding evolution of extracellular moisture. The differences between the k_p cases reflect the different rates at which water is transferred from the intracellular region to the extracellular region.

As k_p increases, intracellular moisture can be supplied to the extracellular region more readily,

In press

modifying the temporal evolution of extracellular moisture and, consequently, the availability of water for evaporation. The temperature response in Fig. 9(b) is coupled with this redistribution. At approximately 60 min, the material temperatures are about 38.8, 40.1, 40.3, and 41.4°C for $k_p = 10^3 k_p^0, 10k_p^0, 10^2 k_p^0$, and $k_p = k_p^0$, respectively.

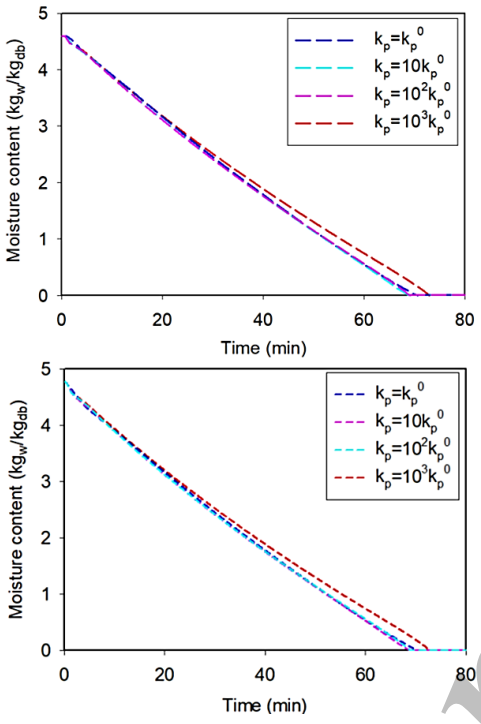


Fig. 8. Graph depicting the simulated temporal variation of (a) intracellular moisture and (b) total moisture content in which kp ranges from the value $k_p = k_p^0$ to $k_p = k_p^0 \times 10^3$

These differences indicate that the rate of moisture supply to the evaporating region affects the intensity of evaporative cooling. In particular, the higher conductivity cases maintain stronger coupling between moisture transport and evaporation for a longer period, delaying the temperature rise associated with the depletion of moisture.

Overall, Fig. 8 and Fig. 9 indicate that the principal role of the water conductivity of the cell membrane is to regulate the redistribution of moisture between the intracellular and extracellular regions and its coupling with the temperature field. The effect on the total drying time is comparatively modest, whereas the effect on intracellular moisture is pronounced. Therefore, variations in k_p should be interpreted primarily in terms of internal moisture redistribution and the resulting thermal response rather than as a direct control of the macroscopic drying rate. The spatial temperature–moisture gradients associated with these redistribution processes are examined separately in Fig. 10.

Another influence that needs to be considered is the relationship between the water conductivity of the cell membrane and the distribution of temperature and moisture content within the sample throughout the drying process. To investigate this, the variation of moisture content X and temperature distribution T as a function of the spatial coordinate at different time points has been obtained from numerical simulations with four different values of k_p varying values. These results are illustrated in Fig. 10, respectively.

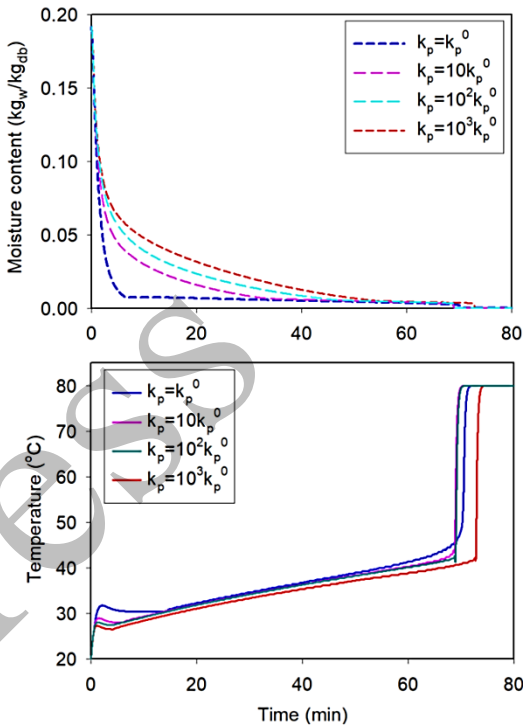


Fig. 9. Graph depicting the simulated temporal variation of extracellular moisture (a) and temperature (b) in which kp ranges from the value $k_p = k_p^0$ to $k_p = k_p^0 \times 10^3$

From Fig. 10, it can be observed that the moisture distribution within the material changes significantly as the value of k_p changes. In the case of k_p small (Fig. 10a), the moisture content across most of the sample thickness is nearly uniform and only decreases significantly in the region near the surface. As the value of k_p increases (Fig. 10b), the moisture gradient along the z-direction becomes more pronounced and the dry material region develops more rapidly from the surface inward, indicating that the moisture transport from the interior to the exterior is enhanced. In the case of k_p large (Fig. 10c), the decline in moisture content occurs more intensely at the surface region and penetrates deeper into the material, indicating that the intracellular moisture diffusion process is significantly enhanced because of the increased moisture release rate at the surface. The variation in the value of k_p also has a pronounced effect on the temperature distribution within the material. In the case of k_p small (Fig. 10d), the temperature distribution is relatively uniform along with the sample thickness and the temperature difference between the surface and the center of the sample is quite small. This can be explained by the low

In press

evaporation rate, which causes most of the supplied thermal energy to be used for heating the entire material. As k_p increases (Fig. 10e), the temperature gradient begins to form more distinctly, with the sample surface tending to be hotter than the interior due to the more intense evaporation occurring in this region. In the case of k_p large (Fig. 10f), the temperature difference between the surface and the center of the sample becomes more pronounced. After the surface moisture content decreases significantly, the temperature at the surface rises rapidly while the interior region still maintains a lower temperature due to the ongoing evaporation process.

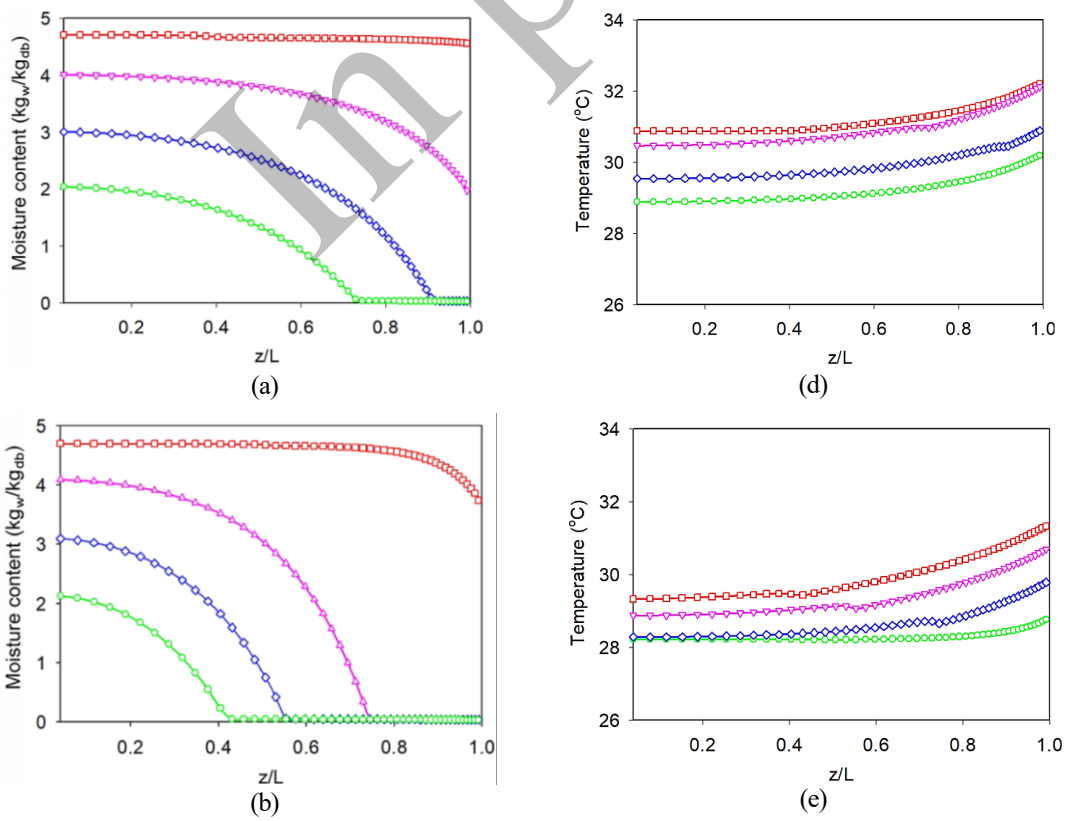
4. Conclusions and Recommendations

In this study, a continuum model for the drying process of cellular plant materials has been developed based on the principles of mass and energy conservation, while accounting for both fluid transport in the intracellular space and moisture diffusion across the cell membrane.

The results show that extracellular moisture evaporates completely during the early stage of the drying process; thereafter, the process is governed by the diffusion of intracellular moisture toward the extracellular vapor. The simulations show that water conductivity of the cell membrane exerts a strong influence on the spatiotemporal distribution of moisture content and temperature within the sample: at low water conductivity of the cell membrane, intracellular moisture is retained near the cell interior and the moisture and temperature profiles along the sample thickness remain markedly non-uniform for most of the process, whereas at high water conductivity of the cell membrane, intracellular moisture is released more rapidly, yielding a more uniform internal distribution and keeping the material temperature closer to the saturation temperature over a larger portion of the drying period. By resolving these two transport pathways explicitly, the model reveals internal distribution behavior — and an associated influence on the predicted drying time — that a conventional single lumped effective-diffusivity model cannot capture, since the latter represents both pathways through one calibrated parameter and is therefore blind to the distinct roles of intracellular and cell membrane transport. This distinction directly addresses the motivation stated in the Introduction regarding the limitation of lumping the transport resistance of both regions into a single effective diffusion coefficient. Although the simulation results demonstrate phenomenologically reasonable trends, the degree of validation of the current model remains limited.

Specifically, model evaluation has thus far been based solely on theoretical framework and idealized assumptions, without a comprehensive and systematic experimental dataset for calibrating and validating the characteristic parameters, which particularly include the water conductivity of the cell membrane at high temperatures. Therefore, the quantitative accuracy and predictive capability of the model under varying operating conditions cannot yet be confirmed with certainty

In press



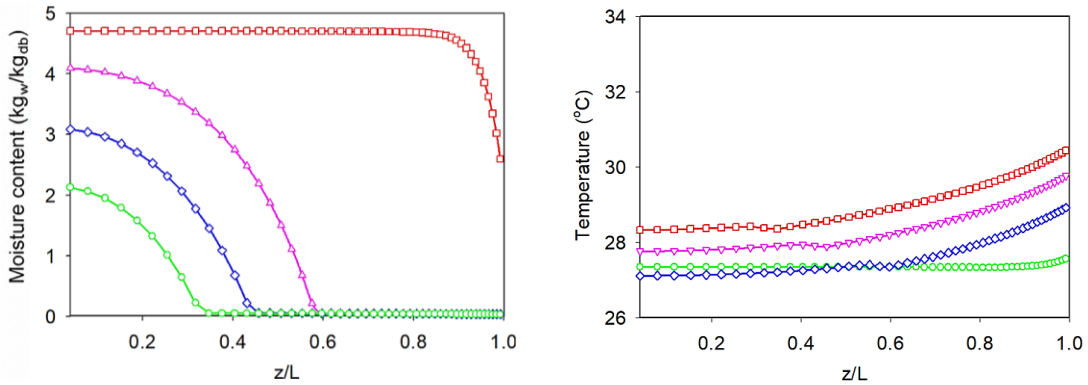


Fig. 10. Simulation results of moisture content (left) and temperature (right) for four different values of water conductivity of the cell membrane (a) (d) $k_p = k_p^0$; (b) (e) $k_p = 10k_p^0$; (c) (f) $k_p = 100k_p^0$ the simulated values are plotted over a time interval of minutes with a time step of $\Delta\tau = 10$ min, the other parameters used in the simulation are $T_f = 80^\circ$C, $w = 0.33$ m/s and $X_0 = 4.8$ kg$_w$/kg$_{db}$

In the future, dedicated experiments will be conducted to collect experimental data on drying kinetics, sample temperature variation, and the relationship between intracellular water potential and moisture content at high temperatures. These data will serve as the basis for parameter calibration and more rigorous model validation, while also enhancing the reliability and practical applicability of the model in the analysis and design of drying processes for cellular plant porous materials. In addition, the simplifying assumptions of the model, which include the neglect of water diffusion between adjacent cells, need to be relaxed in a more advanced model in the future. Under certain conditions, the methodology proposed in this study may be applied to other drying techniques or thermal treatment processes to further elucidate the fluid transport mechanisms under thermal influence in cellular plant porous media. The proposed model is highly complex and is not suitable for direct integration into dryer models that may contain thousands of individual porous material samples. However, since the model is built upon fundamental physical principles, it can be expected to remain valid across a wide range of operating conditio

Table 7 Table of nonenclature

Symbol	Description	Symbol	Description
A_v	specific cell surface area per unit volume, m² m⁻³	ρ	mass density, kg m⁻³
c_p	specific heat capacity at constant pressure, J kg⁻¹ K⁻¹	σ	surface tension, N m⁻¹
d	characteristic pore diameter, m	σ_{rad}	Stefan–Boltzmann constant, W m⁻² K⁻⁴
D_{eff}	effective vapor diffusion coefficient, m² s⁻¹	φ	water potential, Pa
h_{evp}	latent heat of vaporization, J kg⁻¹	ψ	porosity, –
j_w	water flux through the cell membrane, kg s⁻¹ m⁻²	a	dry air
K	absolute permeability, m²	c	capillary
K_r	relative permeability, –	g	gas
k_p	water conductivity of the cell membrane, m³ N⁻¹ s⁻¹	l	liquid
L	thickness, m	$.in.$	intracellular
$\dot{m}$	mass flux, kg s⁻¹ m⁻²	eff	effective
p	pressure, Pa	$conv$	convection
R	universal gas constant, J K⁻¹ mol⁻¹	cr	critical
T	temperature, °C	rad	radiation
t	time, s	sh	shrinkage
v	velocity, m s⁻¹	r	relative
X	moisture content, kg$_w$ kg$_{db}^{-1}$	s	solid

In press

Symbol	Description	Symbol	Description
N	number of spatial nodes, –	v	vapor
α	heat transfer coefficient, W m^{-2} K^{-1}	w	water
δ	thermal emissivity, –	ex	extracellular
ε	volume fraction, –	sat	saturation
λ	thermal conductivity, W m^{-1} K^{-1}	0	initial value
μ	kinematic viscosity, m^2 s^{-1}	f	drying-agent condition

Declarations

Competing interests: The authors declare no competing interests.

References

[1] V. M. Loyola-Vargas and N. Ochoa-Alejo, An Introduction to Plant Cell, Tissue, and Organ Culture: Current Status and Perspectives, in Plant Cell Culture Protocols, 4th ed., New York, NY, USA: Humana Press, pp. 1–3, Jul. 2024. https://doi.org/10.1007/978-1-0716-3954-2_1

[2] G. M. Cooper, The Cell: A Molecular Approach, 2nd ed. Sunderland, MA, USA: Sinauer Associates, 2000.

[3] S. Cichosz and A. Masek, Cellulose structure and property changes indicated via wetting-drying cycles, Polymer Degradation and Stability, vol. 167, pp. 33–43, Sep. 2019. https://doi.org/10.1016/j.polymdegradstab.2019.05.033

[4] P. Perré and I. W. Turner, A mesoscopic drying model applied to the growth rings of softwood: Mesh generation and simulation results, Maderas. Ciencia y Tecnología, vol. 10, no. 3, pp. 251–274, Oct. 2008. https://doi.org/10.4067/S0718-221X2008000300008

[5] N. Vorhauer, T. Metzger, and E. Tsotsas, Empirical macroscopic model for drying of porous media based on pore networks and scaling theory, Drying Technology, vol. 28, iss. 8, pp. 991–1000, Jul. 2010. https://doi.org/10.1080/07373937.2010.497088

[6] G. H. Crapiste, S. Whitaker, and E. Rotstein, Drying of cellular material - I. A mass transfer theory, Chemical Engineering Science, vol. 43, iss. 11, pp. 2919–2928, 1988. https://doi.org/10.1016/0009-2509(88)80045-9

[7] A. Halder, A. K. Datta, and R. M. Spanswick, Water transport in cellular tissues during thermal processing, AIChE Journal, vol. 57, iss. 9, pp. 2574–2588, Sep. 2011. https://doi.org/10.1002/aic.12465

[8] K. H. Le, E. Tsotsas, and A. Kharaghani, Continuum-scale modeling of superheated steam drying of cellular plant porous media, International Journal of Heat and Mass Transfer, vol. 124, pp. 1033–1044, Sep. 2018. https://doi.org/10.1016/j.ijheatmasstransfer.2018.04.032

[9] F. Akter, R. Muhury, A. Sultana, and U. K. Deb, A comprehensive review of mathematical modeling for drying processes of fruits and vegetables, International Journal of Food Science, pp. 1–10, Jul. 2022. https://doi.org/10.1155/2022/6195257

[10] H. T. Vu, Influence of pore size distribution on drying behaviour of porous media by a continuous model, Ph.D. dissertation, Otto von Guericke Universität Magdeburg, Magdeburg, Germany, Jul. 2006.

[11] The MathWorks Inc., MATLAB Version 24.1.0 (R2024a). Natick, MA, USA, 2024. [Online]. Available: https://www.mathworks.com/products/matlab.html. Accessed on: Jun. 17, 2026.

[12] VDI Heat Atlas, 2nd ed. Berlin, Heidelberg: Springer, 2010. https://doi.org/10.1007/978-3-540-77877-6

[13] I. Fatt and H. Dykstra, Relative permeability studies, Journal of Petroleum Technology, vol. 3, iss. 9, pp. 249–256, Sep. 1951. https://doi.org/10.2118/951249-G

[14] Handbook of Industrial Drying, 4th ed. Boca Raton, FL, USA: CRC Press, 2015.

[15] H. T. Vu and T. D. Nguyen, Drying of porous media: an algorithm to determine effective parameters, Vietnam Journal of Science and Technology, vol. 64, no. 2, pp. 28–33, Jun. 2022. https://doi.org/10.31276/VJSTE.64(2).28-33

[16] O. Krischer and W. Kast, Die wissenschaftlichen Grundlagen der Trocknungstechnik, 3rd ed., vol. 1. Berlin, Germany: Springer, 1992.

[17] E. Tsotsas and H. Martin, Thermal conductivity of packed beds: a review, Chemical Engineering and Processing: Process Intensification, vol. 22, iss. 1, pp. 19–37, Jul. 1987. https://doi.org/10.1016/0255-2701(87)80025-9

[18] B. Xiao, J. Chang, X. Huang, and X. Liu, A moisture transfer model for isothermal drying of plant cellular materials based on the pore network approach, Drying Technology, vol. 32, iss. 9, pp. 1071–1081, May 2014, https://doi.org/10.1080/07373937.2014.883629

[19] P. S. Nobel, Physicochemical and Environmental Plant Physiology, 3rd ed. Amsterdam, The Netherlands: Academic Press, 1999.

[20] P. P. Tripathy and S. Kumar, Modeling of heat transfer and energy analysis of potato slices and cylinders during solar drying, Applied Thermal Engineering, vol. 29, iss. 5–6, pp. 884–891, Apr. 2009. https://doi.org/10.1016/j.applthermaleng.2008.04.018

[21] A. N. Califano and A. Calvelo, Thermal conductivity of potato between 50 and 100°C, Journal of Food Science, vol. 56, iss. 2, pp. 586–587, Mar. 1991, https://doi.org/10.1111/j.1365-2621.1991.tb05332.x

[22] Y. Liu, W. Zhu, L. Luo, X. Li, and H. Yu, A mathematical model for vacuum far-infrared drying of potato slices, Drying Technology, vol. 32, iss. 2, pp. 180–189, Jan. 2014, https://doi.org/10.1080/07373937.2013.811687

[23] W. Sutherland, The viscosity of gases and molecular force, Philosophical Magazine, Series 5, vol. 36, iss. 223, pp. 507–531, 1893, https://doi.org/10.1080/14786449308620508

In press